Hole-Collection Mechanism in Passivating Metal-Oxide Contacts on Si Solar Cells: Insights From Numerical Simulations

Ramachandran Ammapet Vijayan [ID], Stephanie Essig, Stefaan De Wolf, Bairava Ganesh Ramanathan, Philipp Löper [ID], Christophe Ballif, and Muthubalan Varadharajaperumal [ID]

Abstract—Silicon heterojunction solar cells enable high conversion efficiencies, thanks to their passivating contacts which consist of layered stacks of intrinsic and doped amorphous silicon. However, such contacts may reduce the photo current, when present on the illuminated side of the cell. This motivates the search for wider bandgap contacting materials, such as metal oxides. In this paper, we elucidate the precise impact of the material parameters of MoO_x on device characteristics, based on numerical simulations. The simulation results allow us to propose design principles for hole-collecting induced junctions. We find that if MoO_x has a sufficiently high electron affinity (≥ 5.7 eV), direct band-to-band tunneling is the dominant transport mechanism; whereas if it has a lower electron affinity (< 5.7 eV), trap-assisted tunneling dominates, which might introduce additional series resistance. At even lower electron affinity, S-shaped J–V curves may appear for these solar cells, which are found to be due to an insufficient trap state density in the MoO_x film in contrast to the expectation of better performance at low trap density. These traps may assist carrier transport when present near the conduction band edge of the MoO_x film. Our simulations predict that performance optimization for the MoO_x film has to target either 1) a high electron affinity and a moderate doping density film or, 2) if the electron affinity is lower than the optimum value, a high defect density not exceeding the doping density inside the film.

Index Terms—Hole collection, passivating contacts, silicon heterojunction (SHJ) solar cell, simulation, transition metal oxides.

I. INTRODUCTION

CLASSICALLY, silicon heterojunction (SHJ) solar cells feature passivating contacts consisting of intrinsic and doped hydrogenated amorphous silicon (a-Si:H) bilayers. These stacked films aim at chemically passivating the crystalline silicon (c-Si) surface [1], while simultaneously inducing a surface potential to enable carrier collection from the wafer [2], [3]. In their simplest implementation, SHJ solar cells feature electron and hole collectors on the opposite sides of the wafer. The a-Si:H layer stacks are usually capped by transparent conductive oxides (TCO) to minimize resistive losses and maximize light coupling into the device [4]. Efficiencies as high as 25.1% have been reported for this type of SHJ solar cells [5]. Although a-Si:H films are quite thin (10–20 nm in total), they can experience significant optical absorption, which can translate to a short-circuit current density (J_{sc}) loss of more than 2 mA/cm^2 in the front hole extraction layers [6].

This loss can be circumvented by placing both contacts on the rear side [7], [8], which has led to the development of single-junction c-Si solar cells with record efficiencies up to 26.7% [9]. An alternative approach that does not require layer patterning to mitigate this loss is to replace the doped a-Si:H with a wider bandgap material with an appropriate work function. A prime example of this approach is the replacement of the a-Si:H(p$^+$) layer with a transition metal oxide (TMO) such as molybdenum oxide (MoO$_x$, x~3) and tungsten oxide (WO$_x$, x~3) [10]–[14], because these materials combine a wide bandgap with a high work function relative to c-Si. The wide bandgap offers good optical transparency whereas the high work function enables hole collection when deposited on c-Si, despite the fact that MoO$_x$ is n-type. As this implies band-to-band transport, such devices will have to rely on efficient quantum-mechanical tunneling of charge carriers or possibly trap assisted. MoO$_x$-based SHJ cells can generate a higher J_{sc} compared with standard SHJ solar cells, though often at the expense of degradation of their fill factor (FF), as evidenced by S-shaped current–voltage (J–V)

TABLE I
MATERIAL PARAMETERS USED IN THE SIMULATION

Material	Parameter	Value
c-Si(n)	Electron affinity	4.05 eV
a-Si:H	Electron affinity	3.9 eV
MoO$_x$	Doping Density	0 to 5×10^{22} cm^{-3}
	Electron Affinity	5.0–6.0 eV
	Effective Density of States	5.065×10^{20} cm^{-3} (for conduction band)*
	Mobility	25 cm^2/V/s (for electrons)*
	Trap Distribution	Uniform density within the bandgap with concentration from 10^{12} to 1.2×10^{21} cm^{-3} eV^{-1} with assumed electron capture cross section* of 10^{-16} cm^2
	Refractive Index	Wavelength-dependent refractive index profile is taken from [41]. Used for optical simulation in AFORS-HET.
TCO	Electron Density	5×10^{20} cm^{-3}
	Electron Affinity	5.5 eV

*Valence band effective DOS, hole mobility, and hole capture cross section have no effect on the results as electron is considered as the charge carrying particle in MoO$_x$ in this paper.

curves [15]–[17]. Understanding the physics underlying hole collection in such contacting stacks is therefore essential for finding strategies to enhance the performance of such devices and passivating-contact solar cells in general.

In this paper, we investigate the charge collection mechanism in passivating contacts featuring TMO-based hole collectors by numerical device simulation using Sentaurus TCAD [18]. In Section II, simulation details are provided and in Section III, we show the individual contribution of doping density, electron affinity, and trap density variations on J–V curves. Later in Section IV, we correlate the understanding gained from Section III with the experimental observations leading to progressive suggestions to attain high efficiency. We also analyse and discuss the components of the current density under the dark and illuminated condition.

II. MODEL AND SIMULATION DETAILS

Work function and bandgap values of MoO$_x$ are taken from the literature [10], [13], [19], [20]. Effective density of states (DOS) for MoO$_x$ film is estimated as 5.065×10^{20} cm^{-3} from the doping density of 10^{18} cm^{-3} [21] and ($E_C - E_F$) difference of 0.16 eV [22]. The reduced Mo oxidation state leads to oxygen vacancies and hence, substoichiometric amorphous MoO$_x$ film [11] which in turn causes n-type doping and gap states in MoO$_x$ film [19], [23], [24] similar to the WO$_x$ film [25]. Even though doping and gap states are interrelated in the MoO$_x$ film, they are considered independently in Section III to understand their individual contribution. The oxygen vacancies which causes n-type doping are shallow donors [26] therefore they are assumed as 100% thermally ionized. The range of doping density variation considered in this paper is shown in Table I.

The nature of the gap states and their distribution in MoO$_x$ are not known prior (to the best of the knowledge of the authors).

Hence, we have chosen these parameters from other contacting materials like a-Si:H [27] and ZnO [28]. To justify the assumptions made, we have conducted wide variations of the values and show that key findings of this work will not be altered (see Appendix A).

We have assumed uniform defect distribution and type of the defects as acceptor (donor) from midgap to the conduction (valence) band edge for simplicity. However, since the trap density discussed in this paper is much lower than the doping density (in most of the cases), the type of the traps does not influence the carrier density considerably and thus band bending and hence, the J–V curve. In addition, the assumed trap assisted tunneling (TAT) transport model is independent of the type of the traps.

We have chosen the value of capture cross section (10^{-16} cm^2) of the traps in the MoO$_x$ film based on the knowledge of reported capture cross sections of defects in a-Si:H film [27] and oxygen vacancy in ZnO [28] which lie in the range of 10^{-15} to 10^{-17} cm^2. However, we have widely varied the capture cross section from 10^{-10} to 10^{-20} cm^2 and illustrated the changes in fitted trap density in Appendix A. The electron mobility is assumed as 25 cm^2 V/s similar to a-Si:H film. However, the variation in electron mobility (from 5 to 1100 cm^2 V/s) has inappreciable influence on FF and hence on fitted trap density as shown in Appendix A. Note that the magnitude of the work function as well as the result of fitting the doping or trap density depend on the estimated DOS and assumed attributes of the defects. Nevertheless, the insights reported here maintain their validity also in case of changes in the assumed/estimated parameters which are summarized in Table I.

For our simulated SHJ solar cell, we take device dimensions and material parameters for a-Si:H and c-Si from [17], [27]. Our model considers carrier transport through an approximately 6-nm thick MoO$_x$ film by two different mechanisms: 1) TAT [18], [29], [30] and 2) drift-diffusion transport. The first mechanism deals with transport via gap states, whereas the second one takes care of electron transport within the bands.

The transport at the MoO$_x$/a-Si:H(i) interface is described by direct and trap-assisted band-to-band tunneling. As trap-assisted band-to-band tunneling at the MoO$_x$/a-Si:H(i) interface happens via gap states in the MoO$_x$ film, we refer to it as gap-state-assisted transport [10], [19]. The model includes only states in the volume of the respective films, i.e., no additional interface-related states. Carrier transport across the TCO/MoO$_x$ interface is simulated by considering both intraband tunneling and thermionic emission.

At the a-Si:H(i)/c-Si(n) interface, we assume that charge carrier transport occurs exclusively by thermionic emission. At the same interface, we set the recombination velocity to the very low value of 10 cm.s^{-1}, representative of actual passivating contact devices. The transport models used in the simulation are sketched in Fig. 1. For the c-Si bulk, state-of-the-art models for radiative recombination, Auger and Shockley–Read–Hall recombination are used from [27]. The optical generation rate of a 150–μm thick textured wafer is calculated using AFORS-HET software [31] and electrical simulations are then carried out using Sentaurus TCAD for a planar solar cell geometry using the charge-carrier-generation profile of a textured wafer.
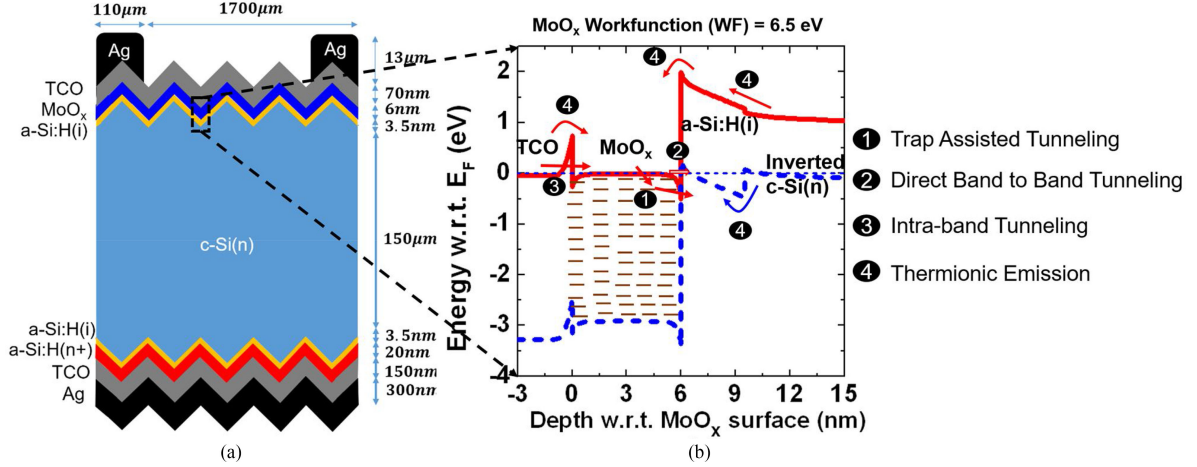
Fig. 1. (a) Schematic diagram of the symmetrical element simulated in Sentaurus TCAD with the geometry described in [27]. (b) Simulated magnified band diagram of the front layers at equilibrium. The thin dashed blue line is the Fermi level (E_F); the thick dashed blue line is the valence band; the solid red line is the conduction band. The small brown dashes in the MoO_x layer indicate that the trap density in MoO_x is assumed to be uniform. The arrows indicate the possible transport mechanisms in the simulation. Their directions correspond to short-circuit conditions under illumination. Inversion of c-Si(n) (the Fermi level near the valence band of c-Si(n)), band sloping in a-Si:H(i), interband overlapping at the MoO_x/a-Si:H(i) interface and the band offset at the TCO/MoO_x interface all depend on the work function of MoO_x.

III. Working Principle of MoOx-Based Solar Cells

A. Hole Collection Mechanism

MoO_x is an n-type material [32]; however, thanks to its high work function relative to the Fermi level of c-Si, it can form a band to band tunneling junction on c-Si acting as a hole collector [13], [33]. Fig. 1(a) and (b) presents a schematic of our simulated solar cell structure and its associated simulated band diagram in equilibrium. Close to the surface, the Fermi level in the c-Si(n) wafer is located near the valence band edge [see Fig. 1(b)]. We observe surface inversion in c-Si(n) induced by the high work function of the overlying MoO_x film.

In Fig. 1(b), we also sketched the assumed uniform trap density in MoO_x as well as a possible transport mechanism in the front stack. From this, a relatively simple device-operation picture emerges: Photogenerated holes are collected toward the front of the c-Si(n) surface, thanks to the induced c-Si surface potential. The collected holes overcome the valence band offset at the a-Si:H(i)/c-Si(n) interface by thermionic emission [34] and recombine at the a-Si:H(i)/MoO_x interface with the electrons injected from the MoO_x layer, either by direct or trap-assisted band-to-band tunneling at the a-Si:H(i)/MoO_x interface. These electrons are injected from the TCO into MoO_x through thermionic or intraband tunneling transport. We can therefore argue that the hole-collection efficiency of MoO_x-based SHJ cells crucially depends on 1) the degree of surface inversion occurring in the c-Si(n) wafer and 2) the absence of transport barriers to charge carriers at the hole contact. Both factors strongly depend on the MoO_x work function, which itself depends on the composition of MoO_x, the deposition technique, and the postdeposition treatment conditions, such as annealing.

B. Work Function Variations

According to experimental studies from the literature, the work function of MoO_x may range from 4.8 to 6.0 eV, depending on the quality of the film and the material interface [23], [35]. In principle, the MoO_x work function ($E_{Vacuum} - E_F$) varies if one alters either 1) the carrier density, which in turn changes $E_C - E_F$, or 2) the electron affinity ($E_{Vacuum} - E_C$). Experimentally, changes in MoO_x work function were reported to be due to carrier density variations (caused by annealing [36]) or electron affinity changes (caused by air exposure [37]). For the sake of comprehensiveness, in this paper, we study the effects of both carrier density (by altering the doping density) and electron affinity changes. For the structure investigated here, we observe that the carrier density is always larger than $\sim 10^{18}$ cm^{-3} even in the doping-less MoO_x film due to charge carrier transfer from adjacent layers as an effect of band alignment.

Fig. 2(a) shows a simulated equilibrium band diagram for MoO_x doping density of 0 and 2×10^{22} cm^{-3} with the possible electron injection shown schematically. The doping density variation from 0 to 2×10^{22} cm^{-3} in this work led the MoO_x film to vary from nondegenerate to degenerate semiconductor regime. Such large doping density is considered in this paper because such large values are required to better explain the experimental data (discussed in Section IV). Now the question is: *Are such large carrier densities in MoO_x films possible at all?* This is supported by comparing the reported conductivity in the range of 10^4 S/cm for the MoO_x film exhibiting semimetallic behavior [when stoichiometry (x) is reduced below 3 [20]] with the conductivity of simulated MoO_x film with the doping density of 2×10^{22} cm^{-3} reaching 8×10^4 S/cm [see Fig. 2(b)]. Such a large doping density causes the Fermi level [see the dashed line in Fig. 2(a)] to move above the conduction band of the MoO_x film [see the blue line in Fig. 2(a)] and hence leads to the reduction in the work function and a decrease of hole accumulation at the front contact. This could be observed from the Fermi level position relative to the valence band edge ($E_F - E_V$) of a-Si:H(i). This finding is replicated in the hole conductivity plot in the a-Si:H(i) layer shown in Fig. 2(b), which shows more than
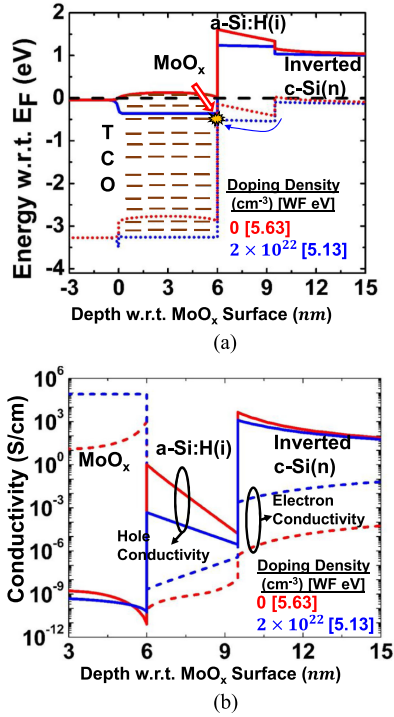
Fig. 2.   (a) Simulated band diagram of a TCO/MoO$_x$/a-Si:H(i)/c-Si(n) contact structure with an MoO$_x$ doping density of 0 cm^{-3} (red) and 2 × 10^{22} cm^{-3} (blue) and a fixed MoO$_x$ trap density of 10^{16} eV^{-1} cm^{-3} and electron affinity of 5.5 eV at equilibrium. (b) Electron (dashed) and hole (solid) conductivities at the MoO$_x$ contact with MoO$_x$ work functions of 5.13 eV (blue) and 5.63 eV (red). The conductivities are for 1-sun illumination and near maximum power point conditions ($V = 0.55$ V).

Fig. 3.   (a) Simulated band diagram of an MoO$_x$ electron affinity of 5.1 eV (blue) and 6.0 eV (red) with a constant MoO$_x$ doping density of 10^{21} cm^{-3} and trap density of 10^{16} eV^{-1} cm^{-3} at equilibrium. (b) Magnified energy band diagram at the interface of MoO$_x$/a Si:H(i) for different MoO$_x$ electron affinities showing no overlap of the conduction band of MoO$_x$ and the valence band of a-Si:H(i) for electron affinity below 5.7 eV. It indicates the change from Type III to Type II heterostructure [39] for electron affinity below 5.7 eV. Black double arrow shows the band overlap for electron affinity of 5.7 eV.

a four order-of-magnitude difference between the two doping cases at the MoO$_x$/a-Si:H(i) interface.

In case of low doping density, the electron conductivity is low in the MoO$_x$ film, however the overall performance is limited by the *hole* conductivity at the a-Si:H(i)/c-Si(n) interface which is lower than the *electron* conductivity in the MoO$_x$ film [see Fig. 2(b)]. Similarly, the figure illustrates the very low electron conductivity in the a-Si:H(i) layer compared with that for holes for a low doping density MoO$_x$ film. It indicates few photogenerated electrons are collected by the hole contact, thanks to the large induced c-Si(n) surface potential in addition to the a-Si:H(i) conduction band gradient [see Fig. 2(a)], which acts as an effective electron barrier. Hence, as suggested in [38], the design rules of high hole conductivity and low electron conductivity to create an ideal hole contact are satisfied by the low doping density (high work function) MoO$_x$ film.

We have then varied the electron affinity, to understand its influence on hole collection mechanism. With *high* electron affinity (≥ 5.7 eV), the modeled energy band diagram in Fig. 3(a) shows a significant overlap of the MoO$_x$ conduction band with the a-Si:H(i) valence band (Type III hetero-structure [39]). In contrast, this overlap is not present for MoO$_x$ with electron affinities *below* 5.7 eV as seen in the magnified energy band diagram in Fig. 3(b) (Type II heterostructure). Our simulation predicts that whenever there is band overlap, carrier transport dominantly occurs by direct band-to-band tunneling. Without band overlap, direct band-to-band tunneling becomes inefficient
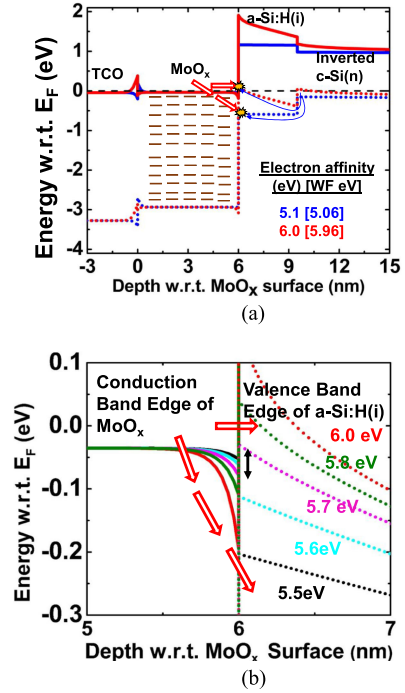
and charge carrier transport occurs by the more resistive trap-assisted mechanism, which in turn depends on the trap density in the MoO$_x$ bulk (discussed in the next section). Despite the large barrier *height* at the MoO$_x$/ITO interface [see Fig. 3(a)], the *width* of this barrier is minimal (<1 nm) enabling easy tunneling through electrons.

The decrease in doping density at constant electron affinity (work function increases) and increase in electron affinity (work function increases) at constant doping density show similar effects on the J–V curve (not shown here). Fig. 4(a) shows the effect of electron affinity variation on the J–V curve. For both high doping concentration and low electron affinity [below 5.5 eV in Fig. 4(a)], in addition to reduction in the surface potential [see Figs. 2(a) and 3(a)], trap-assisted transport is limited which leads to the S-shape in the J–V curves (explained in Section III-C). In case of high doping concentration, large equilibrium capture/emission rates could restrict the availability of the trap to assist the nonequilibrium transport. Similarly, in case of low electron affinity, increase in energy difference between the conduction band of MoO$_x$ and valence band of a-Si:H(i) (see Fig. 3) could restrict the trap-assisted transport. In spite of the difference in the physical mechanisms (for doping and electron affinity variation), both limits the trap-assisted transport (in addition to reduction in the surface potential) and hence manifested as similar effect on the J–V curves. In addition, the decrease in doping density below the trap density deteriorates the J–V curve (see Section III-C) and doping density variation
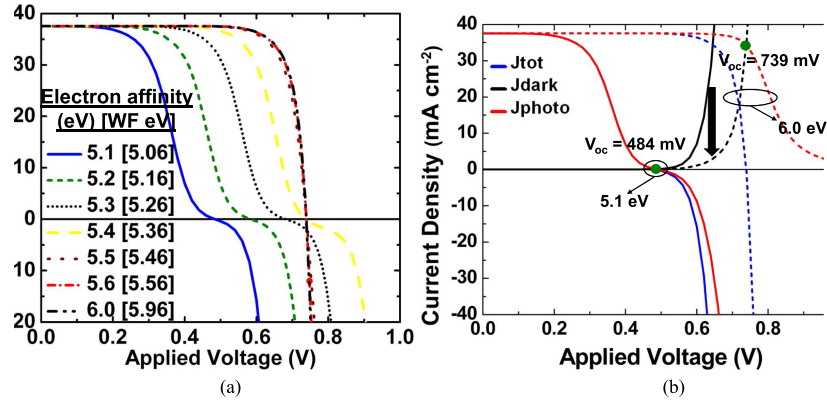
Fig. 4. (a) Simulated *J*–*V* curves under 1-sun illumination for an electron affinity variation (5.1–6.0 eV) with fixed doping density of 10^{21} cm^{-3} and trap density of 10^{16} eV^{-1} cm^{-3}. (b) Extracted photo and dark current dependence on applied voltage for the extreme electron affinity values used in Fig. 4(a). The black arrow in the figures represents the decrease in dark current with respect to increase in electron affinity.
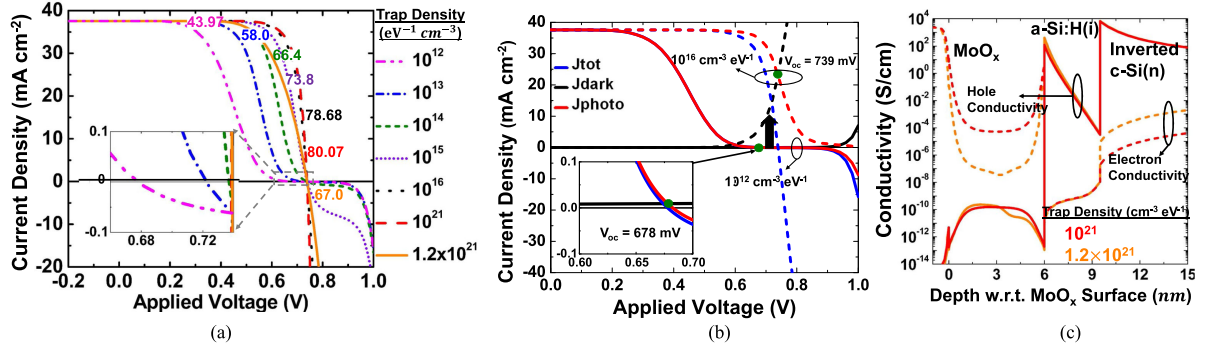

Fig. 5. (a) Simulated *J*–*V* curves for a MoO$_x$ electron affinity of 5.5 eV and doping density of 10^{21} cm^{-3} with different trap densities. The FF values (in %) are shown as labels of the *J*–*V* curves. Since traps are assisting the transport at MoO$_x$ electron affinity below 5.7 eV, the higher the trap density (not exceeding the doping density), the better the performance. The inset shows the V_{oc} points. (b) Extracted photo and dark current dependence on applied voltage for increase in trap density from 10^{12} to 10^{16} eV^{-1} cm^{-3} for other parameters used in Fig. 6(a). The inset shows the V_{oc} point for low trap density as it is difficult to notice in the *J*–*V* curve. The black arrow in the figures represents the increase in the dark current due to the increase in the trap density. The doping density is kept constant as 10^{21} cm^{-3}. (c) Electron (dashed) and hole (solid) conductivities for MoO$_x$ trap densities of 10^{21} eV^{-1} cm^{-3} (red) and 1.2×10^{21} eV^{-1} cm^{-3} (orange). The conductivities are for 1-sun illumination and near maximum power point conditions ($V = 0.55$ V).
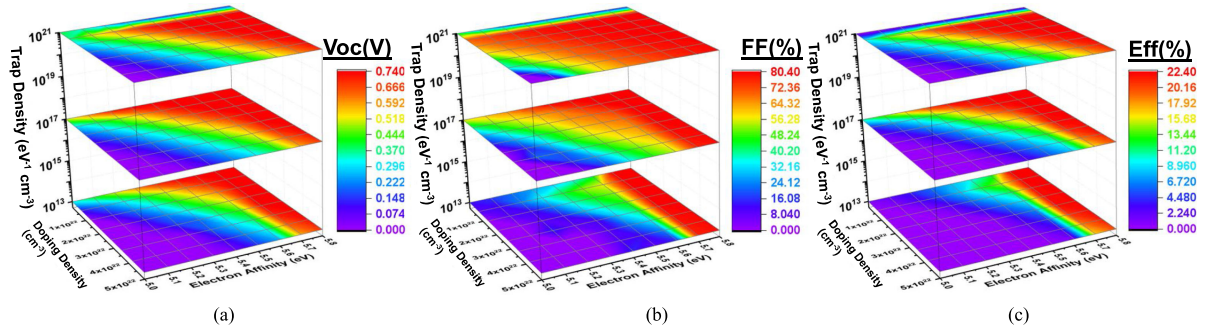

Fig. 6. Three-dimensional surface plot of (a) V_{oc}, (b) FF, and (c) efficiency for the MoO$_x$ doping density, trap density, and electron affinity variations. With an electron affinity above 5.7 eV, both V_{oc} and FF are independent of the trap density (not exceeding the doping density) variations due to the direct band-to-band tunneling transport mechanism. For electron affinity below 5.7 eV, increase in trap densities improves the performance however, high trap densities exceeding doping density degrade the performance independent of the electron affinity value.

for high electron affinity (≥ 5.7 eV) have no significant effect on the *J*–*V* curve (see Fig. 6).

The best performance (high open-circuit voltage, V_{oc}, and FF) is found with the high MoO$_x$ electron affinity (or low doping concentration). V_{oc} drop in the lower MoO$_x$ electron affinity (or higher doping density) devices is attributed to the reduced surface potential (and hence reduced hole inversion and hole conductivity) and increased electron conductivity in the a-Si:H(i) layer. This aspect becomes clear by extracting the dark and photo component [40] from the *J*–*V* curves in
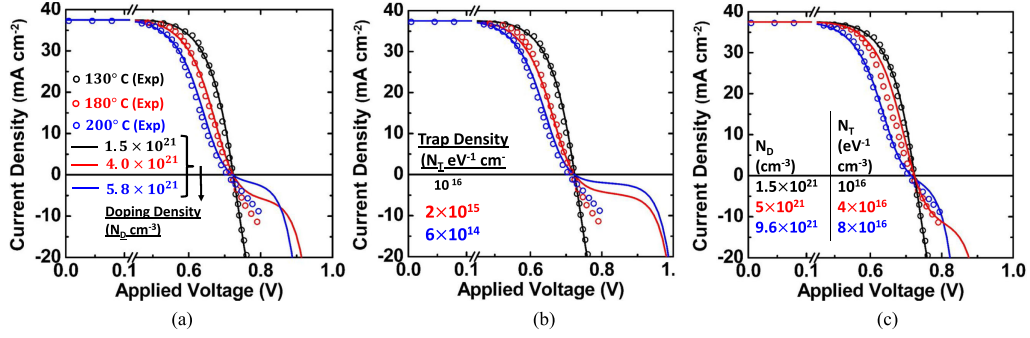
Fig. 7.   With individual variation of single parameters of the MoO$_x$ layer, the reported experimental data (taken from [15]) cannot be reproduced at voltages beyond open-circuit condition. For which (a) the MoO$_x$ doping density or (b) the MoO$_x$ trap density was varied, keeping the respective other parameter fixed (electron affinity = 5.5 eV). (c) Simultaneous variation of both the MoO$_x$ doping density and the trap density matches the experimental data well. Annealing at higher temperatures is reported to increase the trap density [11] and the doping density [23], [35] of MoO$_x$ films. Our simulation shows that when the doping density is increased, the trap density has to be increased for a good fit.

Fig. 4(a) for extreme electron affinity values which is shown in Fig. 4(b).

When the electron affinity increases (or doping density decreases), dark current *decreases* (mainly due to electron current in the a-Si:H(i) layer for voltage below ∼0.8 V) whereas the photo current increases as shown in Fig. 4(b). The significant decrease in the electron current in the a-Si:H(i) from the wafer is due to the significant decrease in electron conductivity (several orders of magnitude) [see Fig. 2(b)] as the hole inversion becomes strong. Hence, a high MoO$_x$ electron affinity or low MoO$_x$ doping density enables an excellent hole-selective contact by inducing a sufficient hole conductivity in the a-Si:H(i) layer along with low electron conductivity.

C. Trap Density Variations

With MoO$_x$ electron affinity values below 5.7 eV, the MoO$_x$ conduction band does not overlap with the a-Si:H(i) valence band (see Fig. 3), causing the charge transport to rely on the MoO$_x$ trap density because the transport is mainly trap assisted. Modeled J–V curves for an MoO$_x$ electron affinity of 5.5 eV and doping density of 10^{21} cm^{-3} are shown in Fig. 5(a) for trap densities from 10^{12} eV^{-1} cm^{-3} to slightly above the fixed doping density 1.2×10^{21} eV^{-1} cm^{-3}. The charge carrier transport is determined by traps near the conduction band edge of MoO$_x$ and the FF increases with the increasing trap density. The V_{oc} increase with trap density is very weak for the considered combination of electron affinity, doping density, and trap density in Fig. 5(a). However, when either the doping density is increased or the electron affinity and the trap density is decreased, V_{oc} dependence on trap density will be apparent [see Fig. 6(a)]. To illustrate this point, we have separated the dark and photo current components shown in Fig. 5(b).

When the trap density increases, both the dark and photo current *increase*, which is relatively straightforward because carrier injection and extraction depends on the trap density. Both FF and V_{oc} increase with the trap density due to the relatively large increase of the photo current compared with the dark current for applied voltage $\leq V_{oc}$ We have observed that FF and V_{oc} dependence on trap density is prominent for lower electron affinity [see Fig. 6(a) and (b)]. This is attributed to the increasing energy

difference between the conduction band of MoO$_x$ and valence band of a-Si:H(i) (see Fig. 3) for lower electron affinity demanding more dependence on trap density.

In spite of the maximum FF value for trap density of 10^{16} eV^{-1} cm^{-3} [see Fig. 5(a)], we have varied the trap density to extremely large values (1.2×10^{21} eV^{-1}cm^{-3}). This is done to show that such large values deteriorate the performance (FF) even without considering Fermi level pinning and parasitic absorption [15], in spite of suggesting that trap density improves the performance.

When the trap density (1.2×10^{21} eV^{-1} cm^{-3}) exceeds the doping density (10^{21} eV^{-1} cm^{-3}) inside the MoO$_x$ film, the electrical performance, especially, the FF diminishes. This is attributed to the poor electron conductivity in the MoO$_x$ film which is lower than the minimum hole conductivity at the a-Si:H(i)/c-Si(n) interface as shown in Fig. 5(c).

Reducing the trap density leads to the appearance of an S-kink in the J–V curves with low electron affinity (see Fig. 4) and consequently to FF degradation. We studied the appearance of the S-kink in the J–V curves in more detail by analyzing the current components. The results show that trap-assisted transport saturates early and switches to thermionic emission with low trap densities (see Appendix B for more details).

Fig. 6 summarizes the effect of doping density, electron affinity, and trap density variations on the V_{oc}, FF, and efficiency. It also shows that *if* a high electron affinity (≥ 5.7 eV) can be guaranteed, the MoO$_x$ trap density (and doping density) does not affect the carrier transport since direct band-to-band tunneling is the dominant mechanism in this case. With MoO$_x$ electron affinity below 5.7 eV, traps are essential for carrier transport, and the higher the trap density (not exceeding the doping density), the better the FF and V_{oc}.

IV. COMPARISON WITH REPORTED EXPERIMENTAL DATA

A comparison of modeled J–V curves and experimental data from an SHJ cell with an MoO$_x$-based front contact that was systematically degraded by thermal annealing [15] is shown in Fig. 7. To fit the simulation to the experimental data, we varied only the MoO$_x$ doping density [see Fig. 7(a)], only the trap density [see Fig. 7(b)], or both [see Fig. 7(c)]. We have done
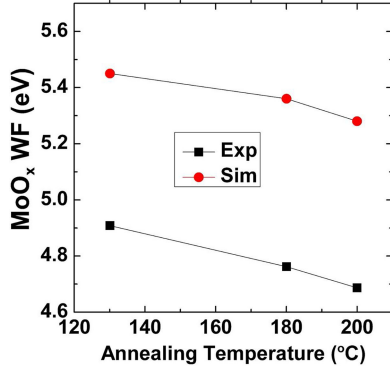
Fig. 8. Comparison of the work function from the fit results in Fig. 7(c) and independently reported experimental data [23] showing a good match in the trends despite the different magnitudes.

this using the prediction from [23] and [36], which states that the doping density increases with the annealing temperature and hence, the work function decreases. When varying only the doping density, we obtained a good match with the experimental data. For the cases with higher MoO_x doping density, however, we see a deviation from the reported experimental data at voltages beyond V_{oc}. Hence, an increase in the MoO_x doping density alone overemphasizes the S-kink in the reported *J–V* curves. When varying only the trap density and maintaining the doping density at a fixed value of 1.5×10^{21} cm^{-3}, there is a strong deviation from the reported experimental data beyond the V_{oc}. From the literature, we know that the work function of the MoO_x film decreases from thermal annealing due to the increase in doping density, whereas the trap density increases due to an increase in oxygen vacancies [11], [23], [36]. Interestingly, simultaneous fitting of the doping density and trap density does provide good agreement with experimental *J–V* curves, as shown in Fig. 7(c). In Fig. 8, we compare the parameters obtained from the simultaneous fit of our simulation results and independently reported work function values from annealed MoO_x films. Despite variations in the magnitude of the work function, which can be caused by the inaccuracy in the used parameters in the simulation (assumed ITO and a-Si:H(i) parameters and effective DOS of MoO_x), the differences in the deposition conditions or device structure (like MoO_x film thickness, ITO properties), the trend is very similar to our simulated result. In summary, our simulation predicts that performance degradation caused by annealing is more likely due to the increase in doping density which in turn reduces the work function. At the device level, this effect is partially compensated since the trap density simultaneously increases, leading to an improved trap-assisted transport mechanism (see Appendix B for more details).

V. CONCLUSION

We conducted numerical simulations of MoO_x-based SHJ solar cells with a focus on the hole collection mechanism. Our simulations show that with an MoO_x electron affinity greater than 5.7 eV, the transport is dominated by direct band-to-band tunneling between the a-Si:H(i) valence band and the MoO_x conduction band when there is an interband overlap. More-
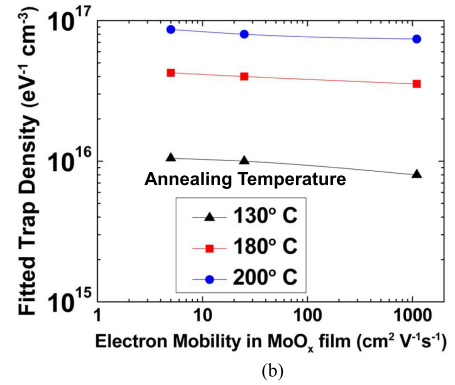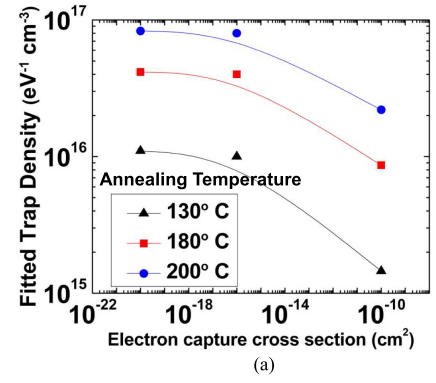

Fig. 9. Influence of (a) electron capture cross section and (b) electron mobility in the MoO_x film on the fitted trap density with the reported experimental data [15].

over, we observe a degradation of FF and the appearance of an S-shape in the *J–V* curves for MoO_x work function below 5.4 eV. We show that both effects are related to charge-carrier transport by TAT, which becomes the dominant transport channel when no direct band-to-band tunneling takes place. Interestingly, FF can be recovered by providing a sufficiently high trap density (not exceeding the doping density), which also removes the S-shape in the *J–V* curve.

In addition, we investigated the origin of the S-shape caused by thermal annealing. When we vary only one parameter, either doping density or trap density, we cannot reproduce experimental results. When we vary both parameters simultaneously, however, excellent agreement between reported experimental *J–V* curves and our simulation is obtained, validating our approach. According to our simulation results, the *J–V* curves of the annealed cells are affected by a lower work function due to an increase in doping density, which also matches with independent experimental observations. This predicts that the reason of the S-shape in annealed MoO_x–SHJ solar cells is their lack of interband overlap (type II heterostructure) MoO_x/a-Si:H(i) interface, which results in transport being limited by less efficient trap-assisted transport. As a general design rule for this kind of solar cells, the TMO electron affinity should be engineered toward being a sufficiently high value while maintaining good electron conductivity. Otherwise, controlling the gap states inside MoO_x could yield better performance in SHJ solar cells with constraints on optical transparency. Having established the fact that annealing reduces the work function of MoO_x in our
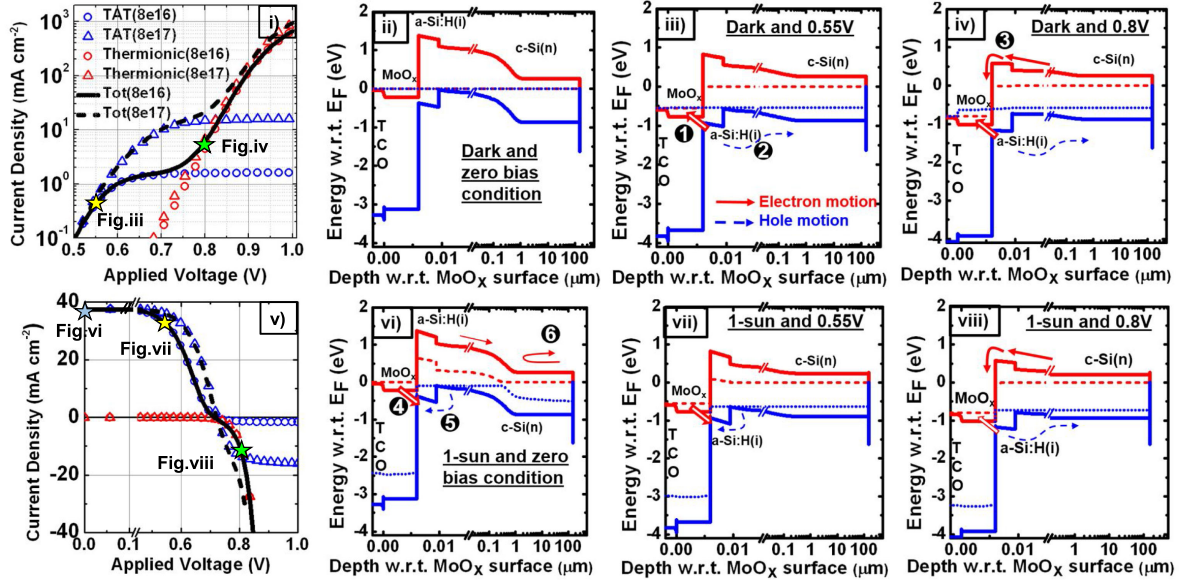
Fig. 10.   i) Dark J–V curve for two trap densities (8×10^{16} eV^{-1} cm^{-3} and 8×10^{17} eV^{-1} cm^{-3}) along with components at the hole contact with a doping density of 9.6×10^{21} cm^{-3}. Corresponding band diagrams without illumination, ii) zero bias, iii) 0.55 V, and iv) 0.80 V along with the dominant carrier motion. v) Light J–V curve for two trap densities (8×10^{16} and 8×10^{17} eV^{-1} cm^{-3}) along with components. Corresponding band diagrams under illumination. vi) Zero bias, vii) 0.55 V, and viii) 0.80 V. The dominant carrier motions are sketched using red (blue) arrows for electrons (holes). The numbers in the figures represent the following carrier actions: 1. Electron extraction from the valence band of a-Si:H(i) through the trap-assisted mechanism. 2. Hole motion using the drift-diffusion mechanism. 3. Electron flow from a conduction band of a-Si:H(i) through thermionic emission. 4. Hole collection using electron injection from MoO$_x$ through the trap-assisted mechanism. 5. Hole collected from c-Si(n) into a-Si:H(i) through thermionic emission. 6. Induced effective electron barrier that keeps the electrons away from the hole contact due to the low electron conductivity.

experimental devices (with associated consequences for the FF), further experiments are required to identify the precise physical cause of the work function reduction.

APPENDIX

A. Influence of Electron Capture Cross Section and Mobility of MoO$_x$ Film on Fitted Trap Density

The fitted trap density in Fig. 7(c) undergo changes when the electron capture cross section and mobility in the MoO$_x$ film is different than assumed in this paper as shown in Fig. 9. Fig. 9(a) shows the increase in capture cross section (compared with assumed value) leads to decrease in the fitted trap density due to the increase in the FF as TAT transport is enhanced. However, the trend (increase in trap density with annealing temperature) remains the same ensuring the validity of the work in spite of wide change in the electron capture cross section. Inappreciable change in the fitted trap density for the wide change in electron mobility shown in Fig. 9(b) might be because the conductivity (and hence FF) is dominated by the carrier density.

B. Current Density Components at the Hole Contact

To understand in greater detail the origin of the S-kink in the J–V curves and to formulate new strategies to enhance device performance, we analyzed the current density components at the hole contact. Fig. 10 shows the results of this analysis for dark and illuminated conditions along with the corresponding band diagrams. We used an MoO$_x$ electron affinity of 5.5 eV, a doping density of 9.6×10^{21} cm^{-3}, and trap densities

of 8×10^{16} eV^{-1} cm^{-3} [fitted parameter in Fig. 7(c) for 200 °C annealing] and 8×10^{17} eV^{-1} cm^{-3}.

Panels i) and v) show the respective components at the hole contacts for dark and illuminated conditions, respectively. These components are trap-assisted and thermionic emission current components. Here, the thermionic emission current relates to electron transport from the conduction band of a-Si:H(i) to the conduction band of MoO$_x$, which is shown in panels iv) and viii). Independent of the dark/illumination conditions, under positive bias conditions below 0.75 V, TAT dominates, whereas under higher bias conditions, thermionic emission dominates. Under dark conditions, electrons are extracted from a-Si:H(i) into MoO$_x$, whereas under illumination conditions, electrons are injected into a-Si:H(i) from MoO$_x$ until V_{oc}. Trap-assisted current becomes saturated at a bias of around 0.7 V, which is the root cause of the S-kink in the J–V curves. The trap-assisted current increases with the increasing trap density [see panels i) and v)], which can be seen from the disappearance of the S-kink in the J–V curves in panel v) [see also Fig. 5(a)]. Hence, the S-kink can be completely eliminated by controlling the trap density especially near the conduction band of MoO$_x$.

Similar studies [40] have been done on an a-Si:H(p$^+$)/a-Si:H(i)/c-Si(n)/Al test structure in which the hole current saturation at the front contact was found to be the key reason for the kink in the J–V curves. In this paper, we show that hole current saturation (the trap-assisted current component) at the front contact can be improved by controlling the trap density in the contacting MoO$_x$ film.

Recently, the reason for the S-kink in MoO$_x$-based solar cell was reported to be due to the band misalignment at the front

contact [17]. In this paper, we show that band alignment at the front contact depends on the MoO_x electron affinity and that tuning subtle parameters like the location of defect (or trap) bands and their concentration in MoO_x film can help to remove the S-kink in *J–V* curves.

REFERENCES

[1] A Descoeudres *et al.*, "Improved amorphous/crystalline silicon interface passivation by hydrogen plasma treatment," *Appl. Phys. Lett.*, vol. 99, no. 12, 2011, Art. no. 123506, doi:10.1063/1.3641899.

[2] W. G. J. H. M. van Sark, L. Korte, and F. Roca, Eds., *Physics and Technology of Amorphous-Crystalline Heterostructure Silicon Solar Cells*. New York, NY, USA: Springer, 2011.

[3] S. De Wolf, A. Descoeudres, Z. Holman, and C. Ballif, "High-efficiency silicon heterojunction solar cells: A review," *Green*, vol. 2, pp. 7–24, 2012.

[4] M. Morales-Masis, S. De Wolf, R. Woods-Robinson, J. W. Ager, and C. Ballif, "Transparent electrodes for efficient optoelectronics," *Adv. Electron. Mater*, vol. 3, pp. 1600529-1–1600529-17, 2017.

[5] D. Adachi, J. L. Hernández, and K. Yamamoto, "Impact of carrier recombination on fill factor for large area heterojunction crystalline silicon solar cell with 25.1% efficiency," *Appl. Phys. Lett.*, vol. 107, no. 23, 2015, Art. no. 233506, doi:10.1063/1.4937224.

[6] Z. C Holman *et al.*, "Current losses at the front of silicon heterojunction solar cells," *IEEE J. Photovolt.*, vol. 2, no. 1, pp. 7–15, Jan. 2012, doi:10.1109/JPHOTOV.2011.2174967.

[7] A. Tomasi *et al.*, "Back-contacted silicon heterojunction solar cells with efficiency>21%," *IEEE J. Photovolt.*, vol. 4, no. 4, pp. 1046–1054, Jul. 2014, doi:10.1109/JPHOTOV.2014.2320586.

[8] K Masuko *et al.*, "Achievement of more than 25% conversion efficiency with crystalline silicon heterojunction solar cell," *IEEE J. Photovolt.*, vol. 4, no. 6, pp. 1433–1435, Nov. 2014, doi:10.1109/JPHOTOV.2014.2352151.

[9] M. A. Green *et al.*, "Solar cell efficiency tables (version 51)," *Prog. Photovolt. Res. Appl.*, vol. 26, pp. 3–12, 2018. [Online]. Available: https://doi.org/10.1002/pip.2978.pdf

[10] C. Battaglia *et al.*, "Silicon heterojunction solar cell with passivated hole selective MoO_x contact," *Appl. Phys. Lett.*, vol. 104, 2014, Art. no. 113902.

[11] C. Battaglia *et al.*, "Hole selective MoO_x contact for silicon solar cells," *Nano Lett.*, vol. 14, pp. 967–971, 2014.

[12] J. Bullock *et al.*, "Efficient silicon solar cells with dopant-free asymmetric heterocontacts," *Nature Energy*, vol. 1, 2016, Art. no. 15031.

[13] M. Bivour, J. Temmler, H. Steinkemper, and M. Hermle, "Molybdenum and tungsten oxide: High work function wide band gap contact materials for hole selective contacts of silicon solar cells," *Sol. Energy Mater. Sol. Cells*, vol. 142, pp. 34–41, 2015.

[14] L. Gerling, S. Mahato, C. Voz, R. Alcubilla, and J. Puigdollers, "Characterization of transition metal oxide/silicon heterojunctions for solar cell applications," *Appl. Sci.*, vol. 5, pp. 695–705, 2015.

[15] J. Geissbühler *et al.*, "22.5% efficient silicon heterojunction solar cell with molybdenum oxide hole collector," *Appl. Phys. Lett.*, vol. 107, 2015, Art. no. 081601.

[16] J. Ziegler *et al.*, "Plasma-enhanced atomic-layer-deposited MoO_x emitters for silicon heterojunction solar cells," *Appl. Phys. A*, vol. 120, pp. 811–816, 2015.

[17] R. V. K. Chavali *et al.*, "A generalized theory explains the anomalous Suns–V_{oc} response of Si heterojunction solar cells," *IEEE J. Photovolt.*, vol. 7, no. 1, pp. 169–176, Jan. 2017, doi:10.1109/JPHOTOV.2016.2621346.

[18] *Sentaurus Device User Manual Version K-2015.06.*, Synopsys, Mountain View, CA, USA, 2015. [Online]. Available: http://www.synopsys.com

[19] M. Greiner *et al.*, "Universal energy-level alignment of molecules on metal oxides," *Nature Mater.*, vol. 11, pp. 76–81, 2011.

[20] J. Bullock, A. Cuevas, T. Allen, and C. Battaglia, "Molybdenum oxide MoO_x: A versatile hole contact for silicon solar cells," *Appl. Phys. Lett.*, vol. 105, 2014, Art. no. 232109.

[21] G. S. Nadkarni and J. G. Simmons, "Electrical properties of evaporated molybdenum oxide films," *J. Appl. Phys.*, vol. 41, no. 2, pp. 545–551, 1970, doi:10.1063/1.1658710.

[22] M. Kröger *et al.*, "Role of the deep-lying electronic states of MoO3 in the enhancement of hole-injection in organic thin films," *Appl. Phys. Lett.*, vol. 95, no. 12, 2009, Art. no. 123301, doi:10.1063/1.3231928.

[23] Z. Zhang *et al.*, "Impact of oxygen vacancy on energy-level alignment at MoO_x/Organic interfaces," *Appl. Phys. Exp.*, vol. 6, 2013, Art. no. 095701.

[24] K. Inzani *et al.*, "Electronic properties of reduced molybdenum oxides," *Phys. Chem. Chem. Phys.*, vol. 19, no. 13, pp. 9232–9245, 2017, doi:10.1039/c7cp00644f.

[25] M. Mews, L. Korte, and B. Rech, "Oxygen vacancies in tungsten oxide and their influence on tungsten oxide/silicon heterojunction solar cells," *Sol. Energy Mater. Sol. Cells*, vol. 158, pp. 77–83, 2016.

[26] Y. Guo and J. Robertson, "Origin of the high work function and high conductivity of MoO_3," *Appl. Phys. Lett.*, vol. 105, 2014, Art. no. 222110, doi:10.1063/1.4903538.

[27] A. Fell *et al.*, "Input parameters for the simulation of silicon solar cells in 2014," *IEEE J. Photovolt.*, vol. 5, no. 4, pp. 1250–1263, Jul. 2015.

[28] D. M. Hofmann *et al.*, "Properties of the oxygen vacancy in ZnO." *Appl. Phys. A, Mater. Sci. Process.*, vol. 88, no. 1, pp. 147–151, 2007, doi:10.1007/s00339-007-3956-2.

[29] A. Palma *et al.*, "Quantum two-dimensional calculation of time constants of random telegraph signals in metal-oxide–semiconductor structures," *Phys. Rev. B*, vol. 56, no. 15, pp. 9565–9574, 1997.

[30] F. Jiménez-Molinos, F. Gámiz, A. Palma, P. Cartujo, and J. A. López-Villanueva, "Direct and trap-assisted elastic tunneling through ultrathin gate oxides," *J. Appl. Phys.*, vol. 91, no. 8, pp. 5116–5124, 2002.

[31] R. Varache *et al.*, "Investigation of selective junctions using a newly developed tunnel current model for solar cell applications," *Sol. Energy Mater. Sol. Cells*, vol. 141, pp. 14–23, 2015.

[32] K. Wong, K. Ananthanarayanan, J. Luther, and P. Balaya, "Origin of hole selectivity and the role of defects in low-temperature solution-processed molybdenum oxide interfacial layer for organic solar cells," *J. Phys. Chem. C*, vol. 116, pp. 16346–16351, 2012.

[33] J. Bullock *et al.*, "Proof-of-concept p-type silicon solar cells with molybdenum oxide local rear contacts," *IEEE J. Photovolt.*, vol. 5, no. 6, pp. 1591–1594, Nov. 2015.

[34] J. P. Seif *et al.*, "Amorphous silicon oxide window layers for high-efficiency silicon heterojunction solar cells," *J. Appl. Phys.*, vol. 115, no. 2, 2014, Art. no. 024502.

[35] J. Meyer, A. Shu, M. Kröger, and A. Kahn, "Effect of contamination on the electronic structure and hole-injection properties of MoO3/organic semiconductor interfaces," *Appl. Phys. Lett.*, vol. 96, 2010, Art. no. 133308.

[36] Y. S. Lin, Y. C Chen, C. M Wang, P. T. Hsieh, and S. C. Shih, "Post-Annealing effect upon optical properties of electron beam evaporated molybdenum oxide thin films," *Appl. Surf. Sci.*, vol. 255, no. 6, pp. 3868–3874, 2009, doi:10.1016/j.apsusc.2008.10.069.

[37] J. Meyer and A. Kahn, "Electronic structure of molybdenum-oxide films and associated charge injection mechanisms in organic devices," *J. Photon. Energy*, vol. 1, no. 1, 2011, Art. no. 011109, doi:10.1117/1.3555081.

[38] U. Wurfel, A. Cuevas, and P. Wurfel, "Charge carrier separation in solar cells," *IEEE J. Photovolt.*, vol. 5, no. 1, pp. 461–469, Jan. 2015.

[39] K. F. Brennan and A. S. Brown, "Semiconductor heterostructures," in *Theory of Modern Electronic Semiconductor Devices*. New York, NY, USA: Wiley, 2002, ch.2, sec. 2.1, pp. 15–16.

[40] R. V. K. Chavali, J. R. Wilcox, B. Ray, J. L. Gray, and M. Alam, "Correlated nonideal effects of dark and light I-V characteristics in a-Si/c-Si heterojunction solar cells," *IEEE J. Photovoltaics*, vol. 4, no. 3, pp. 763–771, May 2014.

[41] B. Macco, M. F. J. Vos, N. F. W. Thissen, A. C. A. Bol, and W. M. M. Kessels, "Low-temperature atomic layer deposition of MoO_x for silicon heterojunction solar cells," *Phys. Status Solidi, Rapid Res. Lett.*, vol. 9, no. 7, pp. 393–396, 2015.

Ramachandran Ammapet Vijayan received the B.E. degree in electronics and communication engineering from Anjali Ammal Mahalingam Engineering College (AAMEC), Thiruvarur, India, in 2009, and the M.E. degree in embedded systems from the College of Engineering, Guindy, India, in 2011. He is currently working toward the Ph.D. degree at the School of Electrical and Electronics Engineering, SASTRA Deemed University, Thanjavur, India.

He worked as an Assistant Professor with AAMEC, from June 2011 to May 2013.

Stephanie Essig received the Master of Physics degree from the Heriot-Watt University, Edinburgh, U.K., in 2008, the Diploma degree in physics from the Karlsruhe Institute of Technology, Karlsruhe, Germany, in 2009, and the Ph.D. degree in physics from the University of Konstanz, Konstanz, Germany, in February 2014, with a thesis on "Development of highly efficient GaInP/GaAs//Si multi-junction solar cells using wafer-bonding" performed with the Fraunhofer Institute for Solar Energy Systems ISE, Freiburg, Germany.

From June 2014 to November 2015, she was a Postdoctoral Researcher with the National Renewable Energy Laboratory, Golden, CO, USA, where her research focused on the development and optimization of Si-based tandem solar cells and passivated contacts for c-Si solar cells. In January 2016, she joined the Photovoltaics and Thin-Film Electronics Laboratory, École Polytechnique Fédérale de Lausanne, Neuchâtel, Switzerland, and was awarded a Marie Skłodowska-Curie postdoctoral fellowship for research on optically transparent carrier-selective contacts and their integration in Si-based tandem solar cells.

Stefaan De Wolf received the Ph.D. degree in electrical engineering from the Katholieke Universiteit Leuven, Leuven, Belgium, in 2005.

During his Ph.D. research, he was also affiliated with IMEC, Heverlee, Belgium, where he worked on crystalline silicon solar cells. From 2005 to 2008, he was with the National Institute of Advanced Industrial Science and Technology, Tsukuba, Japan, where he investigated silicon heterojunction structures and devices. In 2008, he joined the Photovoltaics and Thin-Film Electronics Laboratory, Ecole Polytechnique Federale de Lausanne, Switzerland, as a Team Leader for its activities on high-efficiency silicon solar cells. In September 2016, he became an Associate Professor with King Abdullah University of Science and Technology, Thuwal, Saudi Arabia.

Bairava Ganesh Ramanathan received the Ph.D. degree from Anna University, Chennai, India.

During his Ph.D., he was selected for the Monbusho Fellowship of the Japanese government and worked in the laboratory of Prof. Koichi Kakimoto at Kyushu University, Japan, for two years. He joined Moserbaer Photovoltaic Limited (MBPV), Greater Noida, India, a leading silicon solar cell and module manufacturing company, where he worked as an R&D Manager for four years. He also worked jointly with national and international technical partners in the area of solar cells. He worked as an Assistant Professor for SASTRA Deemed University, Thanjavur, India, from January 2013 to June 2016. He is currently working as a Senior Manager for Mundra Solar PV Limited, Ahmedabad, India.

Philipp Löper received the Diploma degree in physics from the University of Freiburg, Freiburg, Germany, and the Ph.D. degree from the Institute of Microtechnology, University of Freiburg, in 2013, for work on silicon nanocrystal solar cells, which he conducted at the Fraunhofer Institute for Solar Energy Systems, Freiburg.

In 2013, he joined the Photovoltaics and Thin-Film Electronics Laboratory, École Polytechnique Fédérale de Lausanne, Neuchâtel, Switzerland, where he has been working on high-efficiency silicon and silicon-perovskite tandem devices and is heading the group on passivating contacts for silicon solar cells.

Christophe Ballif received the Graduate degree in physics and the Ph.D. degree from the Ecole Polytechnique Fédérale de Lausanne (EPFL), Lausanne, Switzerland, in 1994 and 1998, respectively, focusing on novel photovoltaic materials.

He was a Postdoctoral Researcher with the National Renewable Energy Laboratory, Golden, CO, USA. He was then with the Fraunhofer Institute for Solar Energy Systems, Freiburg, Germany, where he was involved in crystalline silicon photovoltaics (monocrystalline and multicrystalline) until 2003. He then joined EMPA, Switzerland, before becoming a a Full Professor and the Chair with the Institute of Microengineering, University of Neuchâtel, Neuchâtel, Switzerland, in 2004. In 2009, the Institute was transferred to EPFL. He is the Director of the Photovoltaics and Thin-Film Electronics Laboratory in the Institute, as well as the Director of the PV Center, Centre Suisse d' Electronique et de Microtechnique, Neuchâtel. His research interests include thin-film solar cells, high-efficiency crystalline cells, module technology, building integrated photovoltaics, and system aspects contributing to technology transfer and industrialization of novel devices.

Dr. Ballif was the recipient of the Becquerel Prize for Outstanding Merits in Photovoltaics in 2016.

Muthubalan Varadharajaperumal received the M.S. and Ph.D. degrees from Auburn University, Auburn, AL, USA. His Ph.D. research concentrated on simulating the radiation performance of SiGe heterojunction bipolar devices and identification of radiation-hardened layouts for these devices using Sentaurus TCAD, which is being used in space applications at NASA.

After Ph.D. in 2007, he joined the Semiconductor Research and Development Center, IBM, Bangalore as an Advisory Research Engineer. There, he worked on compact modeling of active and passive devices. In 2011, he joined the TCAD department of Global Foundries, Singapore, as a Principal Engineer. He is currently working as an Associate Professor in SEEE, SASTRA Deemed University, Thanjavur, India.